Magnetic Resonance Imaging Duodenoscope

Richard R. A. Syms*, *Senior Member, IEEE*, Ian R. Young, Christopher A. Wadsworth, Simon D. Taylor-Robinson, and Marc Rea

***Abstract*—A side-viewing duodenoscope capable of both optical and magnetic resonance imaging (MRI) is described. The instrument is constructed from MR-compatible materials and combines a coherent fiber bundle for optical imaging, an irrigation channel and a side-opening biopsy channel for the passage of catheter tools with a tip saddle coil for radio-frequency signal reception. The receiver coil is magnetically coupled to an internal pickup coil to provide intrinsic safety. Impedance matching is achieved using a mechanically variable mutual inductance, and active decoupling by PIN-diode switching. ^{1}H MRI of phantoms and *ex vivo* porcine liver specimens was carried out at 1.5 T. An MRI field-of-view appropriate for use during endoscopic retrograde cholangiopancreatography (ERCP) was obtained, with limited artefacts, and a signal-to-noise ratio advantage over a surface array coil was demonstrated.**

***Index Terms*—Duodenoscope, endoscopic retrograde cholangiopancreatography (ERCP), magnetic resonance imaging (MRI), microcoil.**

I. Introduction

THE fiber-optic endoscope, originally developed in the late 1960s, has become the accepted tool for diagnosis and therapy in the upper gastrointestinal tract, including of the biliary and pancreatic ductal systems [1]–[3]. Direct examination, cytology, stone removal, dilation of strictures, and palliative care through intraductal stent placement are all carried out by endoscopic retrograde cholangio-pancreatography (ERCP), a nonsurgical procedure based on the use of a side-viewing flexible duodenoscope equipped with an optical illumination source, video camera, and monitor [4]–[7]. Instruments designed for ERCP also carry a side-opening accessory or biopsy channel, through which a range of disposable catheter tools can be passed.

Manuscript received January 23, 2013; revised April 17, 2013 and May 23, 2013; accepted June 14, 2013. Date of publication June 25, 2013; date of current version November 18, 2013. This work was supported by the Wellcome Trust. *Asterisk indicates corresponding author*.

*R. R. A. Syms is with the EEE Department, Imperial College London, London, SW7 2AZ, U.K. (e-mail: r.syms@imperial.ac.uk).

I. R. Young is with the EEE Department, Imperial College London, London, SW7 2AZ, U.K. (e-mail: youngimarl@aol.com).

C. A. Wadsworth is with the Liver Unit, Division of Diabetes Endocrinology and Metabolism, Department of Medicine, Imperial College London, St. Mary's Hospital, London, W2 1PG, U.K., and also with Aintree University Hospitals NHS Trust, Liverpool, L9 7AL,U.K. (e-mail: c.wadsworth@imperial.ac.uk).

S. D. Taylor-Robinson is with the Liver Unit, Division of Diabetes Endocrinology and Metabolism, Department of Medicine, Imperial College London, St. Mary's Hospital, London, W2 1PG, U.K. (e-mail: s.taylor-robinson@imperial.ac.uk).

M. Rea is with the Department of Radiology, Imperial College Healthcare NHS Trust, St. Mary's Hospital, London, W2 1NY, U.K. (e-mail: marc.rea@imperial.ac.uk).

Digital Object Identifier 10.1109/TBME.2013.2271045

ERCP is primarily used for diagnosis and management of gallstones impacted in the bile duct [8], [9], obstructive jaundice [10], [11], cholangiocarcinoma (cancer of the bile ducts) [12]–[14], and pancreatic cancer [15]–[17]. The patient lies on their side, and the duodenoscope is inserted through the throat and down to the duodenum. Air is used to distend the upper gut and thereby afford luminal views, and water and suction are used to keep the imaging optics clean. The sphincter of Oddi (the point at which the biliary and pancreatic ducts drain into the duodenum in those patients with normal anatomy) is located by endoscopic visualization, and a catheter is then inserted through the sphincter into the common bile duct [18], [19]. This procedure is not straightforward. It is hard to see the sphincter, and even more difficult to locate the bile duct behind it, since the duct is not visible and runs at a highly variable retrograde angle back toward the liver. To minimize the risk of pancreatitis, it is important to avoid inadvertent insertion of a catheter into the pancreatic duct (which is immediately adjacent to and joins the bile duct behind the sphincter) [20]. As a result, ERCP is a demanding procedure with a substantial failure and complication rate. A guidewire system is used to facilitate cannulation and allow multiple catheter insertions without continually encountering the same difficulty [21].

After successful insertion, an X-ray contrast agent containing iodine is injected into the duct [22]. X-ray fluoroscopic imaging then allows the visualization of catheter tools and stents, together with the outline of the duct (and hence any strictures or irregularities). However, owing to the lack of soft tissue contrast, the quality of the images is relatively low and no extraductal imaging is achieved. As a result, X-ray imaging is typically not specific enough to differentiate reliably between blockages caused by gallstones and malignant or nonmalignant strictures. Furthermore, imaging cannot be too extensive; the X-ray dose is limited and medical staff must wear protective aprons and eyewear.

Owing to these difficulties, magnetic resonance cholangiopancreatography (MRCP) is used as an alternative imaging modality for biliary disease, primarily for cholangiocarcinoma [23], [24]. MRCP involves imaging of the ductal system using an external radio frequency (RF) surface coil array, and offers an intrinsic soft-tissue contrast that may be further manipulated using contrast agents. Unfortunately, the relatively large distance between the coils and the tissue of interest yields relatively low signal-to-noise ratio (SNR) at the sub-millimeter-scale resolution required for early diagnosis and accurate staging of cancers such as cholangiocarcinoma. Small internal coils placed close to the field of view (FOV) of interest can have much higher SNR [25], and high-resolution images have been obtained with vascular imaging coils inserted into percutaneous

drainage tubes [26]. However, the procedure is inherently invasive. There is, therefore, a strong case for development of MR-imaging duodenoscopes, to assist with cannulation and carry out high-resolution local imaging of the biliary and pancreatic systems.

A commercial MR-imaging endoscope designed for ^{1}H imaging at 1.5 T and containing a single-turn RF detection coil embedded in its tip (the Olympus XGIF-MR30) was demonstrated in the 1990s [27]–[31], and the development of related coils has continued [32], [33]. A similar research instrument designed for use at 0.5 T has also been investigated. This instrument was initially based on a detached, projecting coil [34], [35] and then on an inductively coupled saddle coil for intrinsic patient safety [36]. Recently, a smaller system containing an expandable RF coil with automatic tuning has been demonstrated [37]. However, the above systems are typically used as colonoscopes or gastroscopes and contain forward viewing optics designed for colorectal or esophageal cancer staging. Furthermore, in some instruments, the biopsy channel was occupied with a back-threaded RF cable, restricting usage to imaging.

In this paper, we describe the development of a fully functioning MR-imaging, side-viewing duodenoscope for use in MRCP. Such instruments present additional challenges because the space available for the RF receiver system is drastically restricted by the optical and mechanical systems required for side viewing and cannulation. The design is introduced in Section II, the hardware development process and the results of electrical testing and magnetic resonance imaging (MRI) are presented in Section III, and conclusions are drawn in Section IV.

II. Instrument Design

The design is based on a 13 mm diameter nonmagnetic side-viewing duodenoscope previously developed by the UK company Endoscan (London, U.K.). This instrument contained a fiber-optic bundle rather than a video camera chip at its tip, to avoid interference between the optical and MR imaging systems. Because the instrument is already extremely complex, the modifications needed to incorporate an RF receiver must be deliberately minimized and achieved without alteration to the clinical functionality. Here the main changes are centered on the instrument tip, with the addition of a sub-miniature cable in the shaft and an RF connector in the handle.

A. Design Overview

A simplified schematic of the tip of the modified instrument is shown in Fig. 1, highlighting the most significant mechanical and optical features. Tip deflection is controlled using wires actuated by operating wheels mounted on the instrument handle. Illumination is provided using a remote white-light source and a fluidic optical fiber. Viewing is carried out using a coherent fiber bundle that routes the image to an eyepiece or a video camera (which can readily be screened from the MR system) on the handle. The optical systems run parallel to the axis through the majority of the instrument, but the light paths are turned through 90° at the tip using prisms to allow side illumination and viewing. An irrigation channel delivers water, air, and suction to clean the imaging optics. A coaxial biopsy channel has its exit in the tip region but is immediately followed by a wire-actuated deflector that is used to achieve the necessary retrograde angle for an emerging catheter.

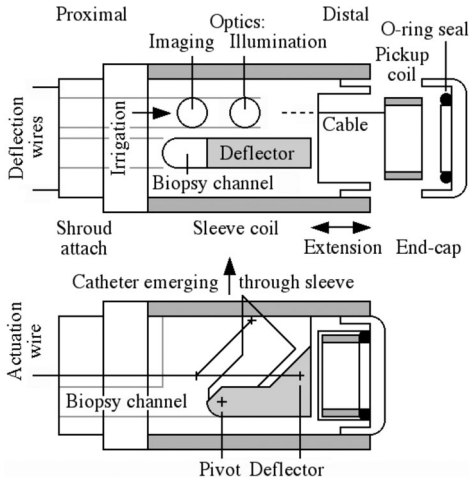

Fig. 1. Schematic diagram of duodenoscope tip, showing the modifications to allow incorporation of an RF receiver for MRI.

The design problem is to incorporate an additional RF receiver in a region already crowded with mechanical and optical systems. The only space available for internal components lies beyond the distal end. However, any significant increase in the length of the tip will reduce its ability to deflect backwards during cannulation. The size of these components must, therefore, be strictly limited. In addition, the receiver system must satisfy several constraints. The first is an MR FOV compatible with the optical FOV, but encompassing the ductal systems hidden from the latter. The second is a local SNR higher than that obtainable using external coils and image uniformity higher than that achievable with a single loop coil. The third is intrinsic patient safety, and the fourth is a simple method of tuning and matching. Additional electrical features must also be accessible for repair, without having to tear down the whole instrument (which is typically built up from the tip to the handle). Consequently, the main receive coil must lie outside the tip, and be detachable for cleaning. Thin-film construction is then imperative, to avoid excessively increasing the final outside diameter. A design satisfying the above constraints was developed for use at $f_0 = 63.85$ MHz (the operating frequency for ^{1}H MRI at 1.5 T).

B. RF Receiver Design

To achieve the first two aims, a single-turn saddle coil enclosing the tip was selected as the imaging coil, in an arrangement close to the Ginsberg–Melchner design (which has 120° angles between conductors and a 2:1 length-to-diameter ratio) [38]. This design achieves the most uniform internal sensitivity in the saddle geometry, and excellent external uniformity. To avoid increasing the tip diameter significantly, this component is fabricated as a thin-film printed circuit board (PCB), consisting of a set of saddle windings with inductance L_1 and resistance R_1

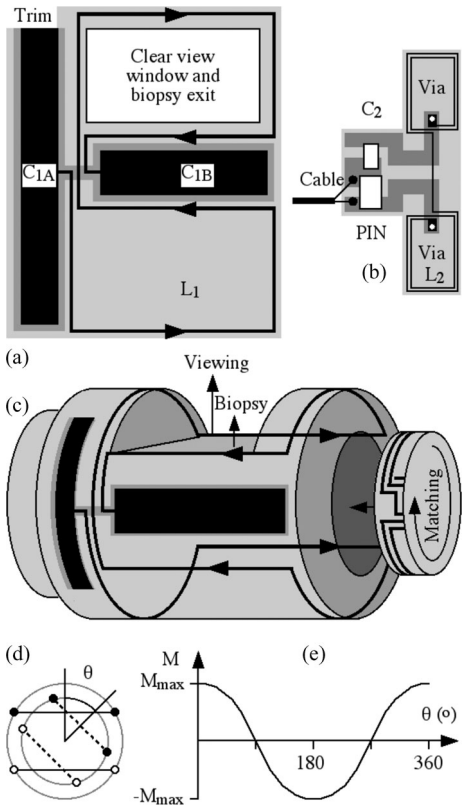

Fig. 2. (a) External coil, (b) internal coil, (c) integration on duodenoscope, (d) variable transformer, and (e) variation of mutual inductance with angle.

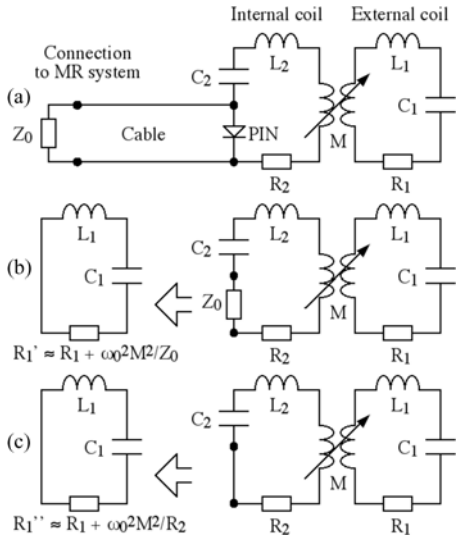

Fig. 3. RF receiver: (a) overall equivalent circuit; (b) PIN diode switch open (receive mode); and (c) PIN diode switch closed (transmit mode).

formed in copper on a flexible polyimide substrate as shown in Fig. 2(a). Other possible coil arrangements, such as the opposed solenoid [39], are certainly candidates. However, because it involves spiral windings, this design cannot easily be implemented in thin film form.

The coil is made resonant at the operating frequency using a pair of parallel plate capacitors $C_{1\mathrm{A}}$ and $C_{1\mathrm{B}}$ that use the substrate as an interlayer dielectric. The overall capacitance $C_1 = C_{1\mathrm{A}}C_{1\mathrm{B}}/(C_{1\mathrm{A}}+C_{1\mathrm{B}})$ is adjusted to set f_0 by trimming $C_{1\mathrm{A}}$ with scissors while measuring the resonance with a network analyzer. SNR in imaging will be determined largely by the unloaded Q-factor $Q_1 = \omega_0 L_1/R_1$ of this coil, where $\omega_0 = 2\pi f_0$ is the angular resonant frequency; good SNR typically requires a Q-factor approaching 100. The use of thin-film circuits instead of conventional inductors and capacitors degrades coil Q-factors, due to the lower conductivity of thin-film copper [40] and the moderate loss tangent of the substrate. However, the reduction is small, and mitigated by constructional simplicity. The circuit is embedded in a plastic sleeve with an opening to allow unobstructed optical imaging and catheter passage. The external coil is held in place using a spring clip, and is removable for cleaning.

To achieve the third aim, the arrangement used by Gilderdale *et al*. [36] was adopted. This design avoids any direct connection to the outer coil by mutual coupling to a smaller internal coil, and hence provides intrinsic patient-system isolation. The use of an entirely removable coil also allows thorough cleaning between patients. The internal coil is mounted in a cavity, which leads to a cable run alongside the imaging fibers. RF signals are routed via miniature coaxial cable, and connected to a connector on the operating handle. The internal coil remains *in situ* during cleaning, but can be removed for repair by removing an end-cap. This coil is again a thin-film PCB, arranged as a two-turn thin-film saddle coil with inductance L_2 and resistance R_2, as shown in Fig. 2(b). Two discrete components (a surface mount capacitor C_2 used to make the coil resonant at the operating frequency and a PIN diode used to control decoupling) are mounted on the PCB. The internal coil is wrapped around a cylindrical plastic shell and the PCB folded to place the components inside the shell.

The overall placement of the two coils is shown in Fig. 2(c). The external and internal coils are arranged to overlap, so the two have a mutual inductance M. In contrast to [36], the use of a saddle pickup allows M to be adjustable if the internal coil is rotated about the instrument axis, as shown in the end-on view of Fig. 2(d). M will have its maximum value $M_{\max}$ when the relative angle θ between the coil axes is zero, falling to zero when $\theta = 90^\circ$ and reaching a minimum $-M_{\max}$ when $\theta = -180^\circ$. More generally, M will vary approximately cosinusoidally with θ, as shown in the sketch of Fig. 2(e), following $M \approx M_{\max} \cos(\theta)$.

C. Impedance Matching and Decoupling

Matching and decoupling followed a simplified version of the approach used in [36]. The equivalent circuit of the receiver is as shown in Fig. 3(a), where external loading is neglected for simplicity. It is assumed that the output is connected to an MRI scanner, which has impedance Z_0 via a cable of similar impedance. It is also assumed that the scanner provides a dc voltage to hold the PIN diode in reverse bias during the signal reception phase of MRI. In this case, it appears as a small capacitance approximating an open circuit as shown in Fig. 3(b). Although the circuit is technically doubly resonant, the Q-factor

of the internal coil is low at this point. To good approximation, the circuit appears singly resonant, and inductive matching effectively inserts a resistance $\omega_0^2 M^2/(Z_0+R_2)$ into the external resonator at ω_0. Since Z_0 will typically be much larger than R_2, the second term in the denominator may be neglected. The effective resistance of the external resonator is then $R_1' = R_1 + \omega_0^2 M^2/Z_0$.

If $\omega_0 M$ can be made equal to $\sqrt{(R_1 Z_0)}$, impedance matching can be achieved directly. This condition is extremely helpful in simplifying construction. However, tight coupling between the coils is required to achieve suitably high values of $\omega_0 M$. Assuming that $R_1 \approx 0.5\ \Omega$ and $Z_0 = 50\ \Omega$, we require $\omega_0 M \approx 5\ \Omega$. If $\omega_0 M_{\max}$ is chosen to be slightly larger than this value, exact matching can then be achieved by rotating the internal coil to decrease M. At this point, $R_1' = 2R_1$.

The effect of a lossless matching network is to convert the signal source into one of output impedance Z_0, which may therefore be matched effectively to the load. In this case, the network has an additional series resistance R_2 that degrades the SNR. However, assuming $R_2 \approx 0.5\ \Omega$ and $Z_0 = 50\ \Omega$ the SNR penalty is extremely small and likely to be similar in an external isolation transformer.

It is also assumed that the scanner provides a dc current to drive the PIN diode into forward bias during the excitation phase of MRI. In this case, it appears as a small resistance approximating a short circuit, as shown in Fig. 3(c). The complete circuit then acts as a coupled resonator system, with split resonant frequencies. However at ω_0, the internal circuit effectively transfers resistance into the external one, whose total resistance is then given by $R_1'' = R_1 + \omega_0^2 M^2/R_2$. Assuming the circuit is matched as described earlier, $\mathrm{R}_1'' = R_1 + Z_0 R_1/R_2$. Since R_1 and R_2 are similar, the first term may be neglected and we may take $R_1'' \approx Z_0 R_1/R_2$. This increased resistance significantly reduces any current directly induced during the excitation phase of MRI. The ratio between the currents resulting from any induced voltage in the transmit and receive states is $R_1'/R_1'' \approx 2R_2/Z_0$. For the resistance values above, induced currents are reduced by a factor of ≈50 or around 35 dB.

Prioritization of patient-system isolation does unfortunately lead to a reduction in the effectiveness of the decoupling, due to the use of an unshielded internal coil. For example, solution of the circuit equations shows that the small current I_1 in the external coil is accompanied by a larger current I_2 in the internal coil, with relative magnitude $|I_2|/I_1 = \sqrt{(R_1 Z_0)}/R_2$. For the resistance values above, this ratio is 10. This current may clearly induce flip angle artifacts. However, its effect is mitigated by the small size of the internal coil, which is buried inside the instrument. Furthermore, during excitation, voltages may also be induced directly in the internal coil. The resulting current I_2 may, in turn, give rise to a larger current I_1 in the external coil, with relative magnitude $|I_1|/I_2 = \sqrt{(R_1 Z_0)}/R_1$. However, because of the much smaller surface area of the internal coil, the induced voltage is much lower.

Since the external and internal coil rejection ratios depend on Z_0 and $\sqrt{Z_0}$, respectively, increased rejection can be achieved for both coils by inserting a matching network between the cable and the PIN diode to raise the apparent value of Z_0 [36]. However, this approach requires additional circuit components. Furthermore, an increase in $\omega_0 M$ is required for matching, which, in turn, increases R_2. As a result, iteration is again required to achieve a significant improvement in performance. Owing to the inherent space constraints, these complications were avoided. Further difficulties are introduced by external loading, which detunes the external coil and alters the matching condition. To cope with a range of loading conditions, the external coil may be tuned slightly above the MRI frequency and the internal coil arranged to match to a slightly higher resistance.

One further point deserves mention. There are many reports of heating of long conductors during MRI (e.g., see [41]), due to excitation of standing waves by the strong electric field of transmitter coil capacitors. The effect is highly significant during intravascular procedures, when conductors with a thin insulating layer are closely surrounded by tissue with a high dielectric constant, and the resonant length is therefore very short. Although long conductors such as the coaxial output are present in an endoscope, these are surrounded by a much greater thickness of material with a low dielectric constant. Furthermore, the surrounding tissue is likely to be in less intimate contact during endoscopy, especially if air is used to ease the passage of the instrument. As a result, the resonant length will be much longer and the electrical and thermal insulation much greater. There have been no reports to date of problems with MR imaging endoscopes operating at 1.5 T.

III. Construction and Evaluation

Several iterations were required to implement the design concepts mentioned earlier. Particularly, optimization of the overlap between the internal and external coils was required to achieve a suitable value of $\omega_0 M_{\max}$. To avoid contamination (and subsequent difficulties with obtaining authority to use the instrument in patients), these iterations and their evaluations were carried out using a dummy duodenoscope tip before proceeding to a complete instrument.

A. Thin Film Circuits

Thin film circuits were fabricated by double-sided patterning of copper-clad polyimide by the U.K. company Clarydon (Willenhall, West Midlands, U.K.). The starting material was 25 μm thick Kapton HN (DuPont, Circleville, OH, USA), coated on each side with a 35-μm-thick pressure-bonded layer of copper and patterned by lithography and wet etching. Track layouts were established by a combination of iteration and numerical simulation. Circuits were fabricated in arrays with coils of different length to allow optimization of $\omega_0 M_{\max}$. However, the internal coil had a track width and track separation of 500 μm throughout, while the external coil had a track width of 650 μm. The circuits were separated using a scalpel, and mounted on cylindrical mandrels formed in polyether–ether–ketone (PEEK) for testing.

Electrical evaluation was carried out using an Agilent E5061 A electronic network analyzer (ENA). Frequencies and quality factors of resonators were established using inductive probes for input and output coupling. Inductances were

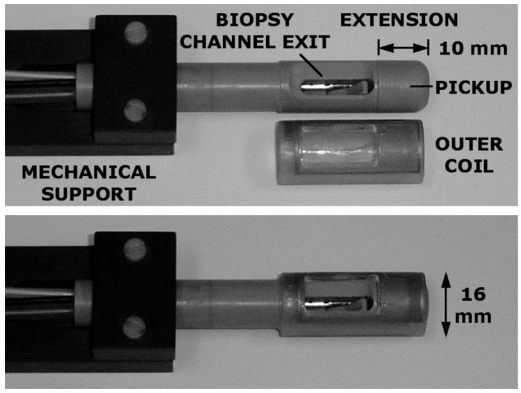

Fig. 4. Dummy duodenoscope tip with biopsy channel, catheter deflector, and RF receiver.

established by making coils resonant with known capacitors, and resistances were found from quality factors. Internal capacitances were found from resonant frequencies and inductances, and mutual inductances were found from resonance splitting in coupled systems.

The internal pickup was constructed from a 9-mm-long two-turn saddle coil, with diameter 8 mm. The via connections needed to complete the circuit were first formed by soldering through pinholes, and the coil was then tuned to the resonant frequency using two nonmagnetic capacitors totaling 50.3 pF (SRT Micro Céramique, Vendome, France). The unloaded Q-factor was measured as 75. These data imply an inductance L_2 = 123.5 nH and a resistance $R_2 = 0.66\ \Omega$. A MA4P7464 F-1072 nonmagnetic PIN diode (M/A-COM Technology Solutions, Lowell, MA, USA) and a length of 2.2 mm diameter nonmagnetic coaxial cable (Axon Cable, Dunfermline, U.K.) were then added.

The external coil was constructed from a 31-mm-long single-turn saddle coil, which was mounted on a 100-μm-thick cylindrical sleeve with diameter of 13 mm and tuned to frequency by trimming C_{1A}. The circuit was then encapsulated in epoxy resin and machined to achieve a cylindrical shape and form the viewing slot. To avoid significant alteration to the resonance due to loading, an encapsulation thickness of 1.5 mm was used, increasing the tip diameter to 16 mm. The resonant frequency was set slightly high, to compensate for the effect of loading. The coil parameters were extracted as $L_1 = 140$ nH, $C_1 = 43.5$ pF, $Q_1 = 90$, and $R_1 = 0.6\ \Omega$.

B. Dummy Duodenoscope

The dummy duodenoscope contained an internal receiver cavity and a biopsy channel with an operating catheter deflector, as shown in Fig. 4, but omitted all illumination and imaging optics. The tip itself was fabricated in PEEK and titanium, and mounted on a Delrin (polyoxymethylene) mechanical support that routed the biopsy channel, deflector wire, and signal cable to a simplified handle. The internal cavity required a tip extension of ≈10 mm. Before insertion, the internal PCB was simply wrapped around a cylindrical PEEK spring, and the output cable was routed through the in-built cable run.

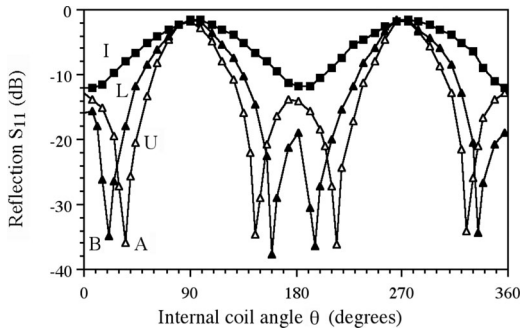

Fig. 5. Variation of reflection with internal coil angle, unloaded, loaded, and immersed in tissue-simulating solution.

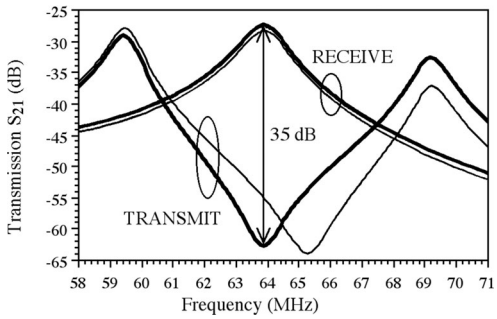

Fig. 6. Frequency responses of the RF circuit in receive and transmit states, measured at the receiver midpoint (thick lines) and distal tip (thin lines).

The internal coil was then rotated to set M to the value needed for impedance matching. Different values of θ were required for different loads, which alter the effective value of R_1. For example, curve U in Fig. 5 shows the variation of the reflection coefficient S_{11} with θ, with the receiver unloaded. Here the reflection is -12 dB when $\theta = 0$, but may be reduced to a minimum when $\theta = 35^\circ$ (condition A, the impedance matching point). Curve L shows similar results with the receiver loaded by a large copper plate. Once again, the system may be matched, but at a smaller value of θ (condition B). Finally, curve I shows results with the receiver heavily loaded by immersion in a tissue simulating solution (3.37 g/L $NiCl_2{\cdot}6H_2O$ and 2.4 g/L NaCl with T_1 = 500–800 ms and T_2 = 100–200 ms). Here the additional load is so large that $\omega_0 M_{\max} < \sqrt{(R_1 Z_0)}$ and exact matching cannot be achieved. For "average" loads, the best compromise is condition B. The cap was sealed, and the external coil locked in place.

The performance of the assembled receiver was assessed, by measuring the overall system transmission S_{21} in receive and transmit states (using a signal generator to provide a low-frequency control voltage, a large wire loop to simulate uniform RF excitation, and a small wire loop as a local current probe). Fig. 6 shows the transmission, measured at the midpoint of the external coil (thick lines) and the distal tip near the internal coil (thin lines). In the receive state, the circuit is singly resonant with a loaded Q-factor of 30. In the transmit state, the circuit is doubly resonant. Near the coil midpoint, the signal rejection is 35 dB at ω_0, broadly in agreement with the design analysis; however, the rejection is noticeably worse at the tip due to the unwanted

currents discussed earlier. Similar results were achieved with the tip immersed in a tissue simulating solution but with a slight downshift in frequency and a reduction in the loaded Q-factor to 20. From the Q-factors measured when the coil is dry and immersed, and the condition that the impedance mismatch is roughly the same in each case, the output impedance of the receiver may be estimated as 30 Ω (unloaded) and 70 Ω (heavily loaded).

C. Magnetic Resonance Imaging

The performance of the receiver was verified by MRI at St Mary's Hospital, Paddington, London, using a 1.5 T Signa Excite clinical scanner (GE, Milwaukee, WI). Initial imaging was carried out using a spin echo sequence with TR = 520 ms and TE = 8.6 ms. The body coil was used for excitation, and the duodenoscope receiver was connected to an auxiliary coil input for signal reception. Decoupling and signal reception were assessed first, by imaging with the dummy duodenoscope tip immersed at a shallow angle in tissue-simulating solution. A catheter was also passed through the biopsy channel to mimic cannulation. This arrangement is particularly challenging, since the receiver system is heavily loaded by salt solution surrounding the external coil, and also by the solution penetrating the biopsy channel. However, it provides an extremely direct method of visualizing and assessing performance.

Fig. 7(a) shows quasi-axial images of the receiver tip in the region of the catheter deflector, obtained in a block of 18 slices using 3 mm slice thickness and 4 excitations (NEX). Here the image resolution is 0.78125 mm/pixel, and the image bandwidth is 162.734 Hz/pixel. The left-hand (LH) half shows an image obtained using the body coil in the vicinity of the catheter deflector. This image is generally bright, except in the region where the signal source is occluded by the tip. There is some perturbation to the magnetization near the four coil conductors, and also the 1 o'clock position to the right of the catheter. Both are indicative of a failure of decoupling, whose effectiveness is limited by the need to minimize the length of the tip extension and further degraded by the heavy saline loading. Improvement of the former would require design alterations, but the loading is likely to decrease during actual use. The right-hand (RH) half shows the corresponding image obtained using the duodenoscope receiver. Since the sensitivity of a saddle coil varies with distance, a radial correction factor has been applied to the image outside the coil diameter; a similar correction has been applied to all subsequent axial images.

Fig. 7(b) shows corresponding sagittal images, obtained in a block of 18 slices using a 2 mm slice thickness and 4 NEX. The LH half shows a slice through the plane of the catheter obtained using the body coil, while the RH half shows the corresponding image obtained using the duodenoscope receiver. In the former case, it is clear that there is a small perturbation to the magnetization above and below the tip. In the latter, the internal structure of the tip (including the biopsy channel, catheter deflector and catheter) is well resolved, despite the short acquisition time (1 min 48 s). However, a characteristic pattern of

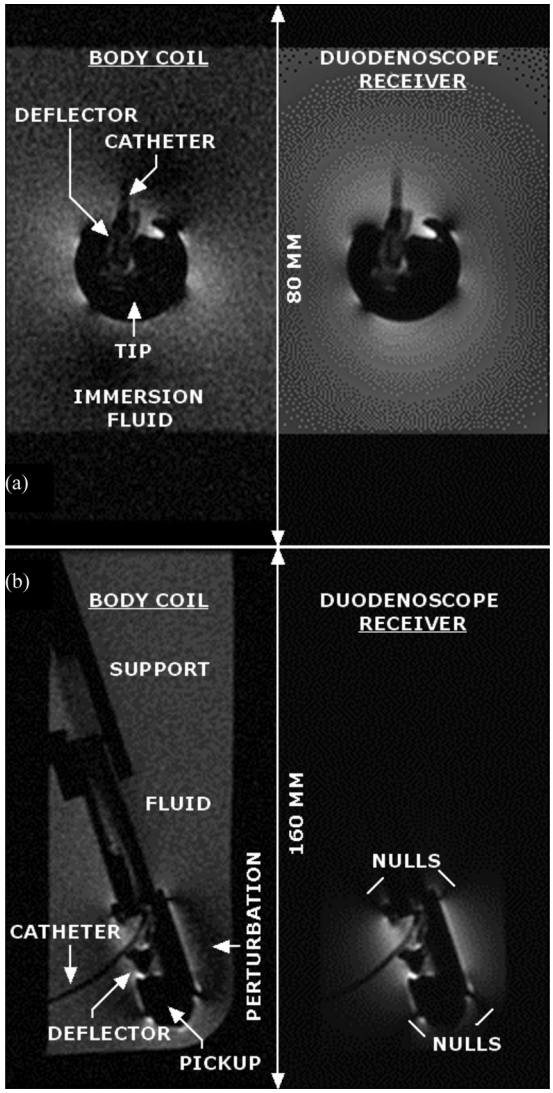

Fig. 7. (a) Quasi-axial and (b) sagittal slices across the immersed tip, obtained using the body coil (LH) and the duodenoscope receiver (RH). $1/R$ scaling has been applied to the duodenoscope axial image.

signal nulls associated with the saddle coil geometry may be seen, behind and in front of the coil.

The spatial sensitivity of particular coil configurations may be estimated via reciprocity [42]. Computed contour maps of constant RF field magnitude obtained from a driven saddle coil may be found in papers by a number of authors, e.g., [43]. For the transverse midplane, these show approximately uniform patterns, falling off roughly as $1/R$. Because the driven field is approximately radial for this important plane, the usual cosine factors would be expected when the coil lies at an angle with respect to the B_0 field. X-ray fluoroscope images show duodenoscope tips typically lying between 5° and 40° with respect to the spine during cannulation at ERCP, and hence in this angular range with respect to the magnet bore. Under these circumstances, the cosine factors will make relatively small difference to the sensitivity. To verify that usable images may still be obtained, the coil axis was chosen to lie at $\approx 20°$ with respect

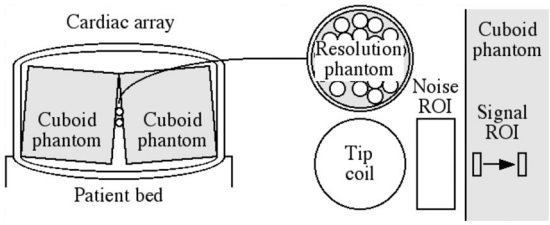

Fig. 8. Overall and enlarged views of the arrangement for comparison of eight-element surface array coil and duodenoscope receiver.

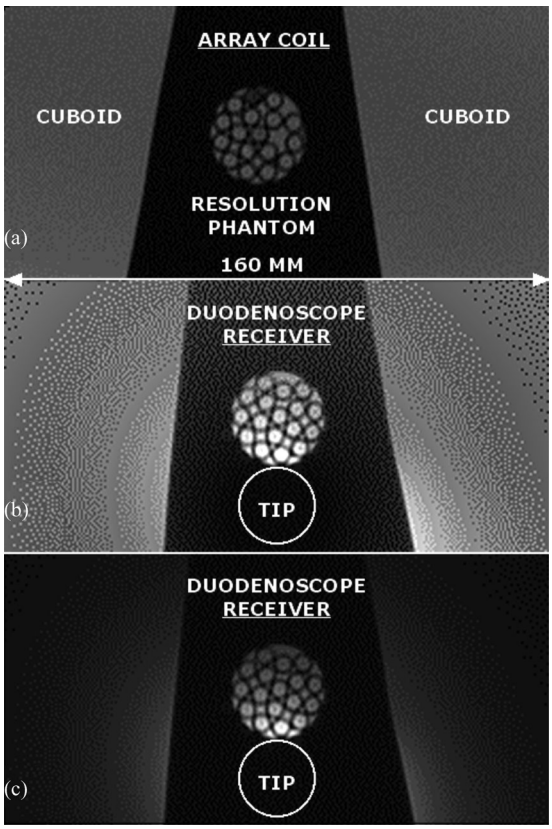

Fig. 9. Axial slices across resolution test phantom obtained using (a) the eight-element cardiac array coil, and (b) and (c) the duodenoscope receiver, with and without $1/R$ scaling.

to the B_0 field in Fig. 7(b). However, images have also been obtained at larger angles.

D. Image Quality

Image quality was then assessed quantitatively by comparison with an eight-element GE HD cardiac array coil in the arrangement of Fig. 8. A resolution phantom consisting of a 14 mm ID tube filled with smaller tubes with 0.4 mm wall thickness immersed in tissue simulating solution was placed between two cuboid phantoms. The arrangement was then imaged using the array and the duodenoscope receiver in turn.

Fig. 9 shows axial images across the phantom arrangement, acquired in a block of 13 slices, 2 mm slice thickness and 2 NEX (requiring a total acquisition time of 2 mins 49 s). Here the image resolution is 0.3125 mm/pixel, and the image bandwidth is 81.367 Hz/pixel. Fig. 9(a) shows an image obtained using

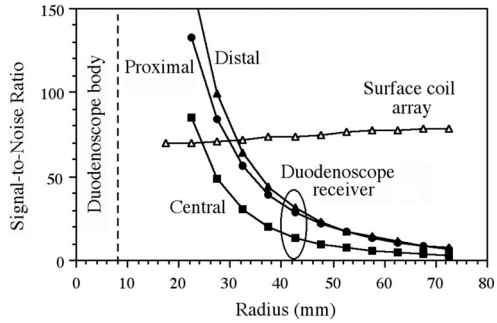

Fig. 10. Spatial dependence of SNR for duodenoscope receiver at different longitudinal positions (circled) and surface array coil.

the array, and Fig. 9(b) and (c) shows the corresponding image obtained using the duodenoscope receiver, with and without $1/R$ scaling, respectively. In each case, the details of the resolution phantom are clearly visible. The duodenoscope receiver clearly provides increased brightness, but over a limited field of view. The use of $1/R$ scaling can reduce the dynamic range required for display, but clearly cannot mitigate the reduction in SNR at large distance.

Using images of this type, the SNR of the two coil systems was compared. Noise was estimated from a large region of interest (ROI) nominally devoid of signal, while signal was estimated from a small ROI moving radially away from the instrument tip as shown in Fig. 8. Fig. 10 shows the variation of SNR for the duodenoscope receiver with radius R, measured at different points along the tip.

SNR is higher near the proximal and distal circumferential conductors of the saddle coil and lower at the central point between. However, in each case SNR falls off approximately as $1/R$. Also shown is the corresponding data for the surface coil array. In this case the SNR is approximately constant. The duodenoscope receiver provides a higher SNR to a radius of at least 25 mm, suggesting a useful imaging volume.

E. Ex Vivo Imaging

Tissue imaging was demonstrated using a conventionally butchered *ex vivo* porcine liver. Porcine anatomy differs from human anatomy in having the bile duct enter the duodenum separately from the pancreatic duct, 2–5 cm distal to the pyloric sphincter at the end of the stomach (also known as the *torus pyloricus* or pyloric ring) [44]. A liver specimen was obtained from an abattoir, with attached gall bladder, biliary ductal system, and a section of duodenum. The duodenum was opened with a scalpel to identify the *torus pyloricus*, sphincter, and bile duct. The bile duct was filled with water using a syringe, the duodenoscope receiver (covered with a latex sheath) was then positioned and the duodenum folded over.

Imaging was carried using a three-dimensional (3-D) gradient recalled sequence with a repeat time TR $=$ 33 ms, an echo time TE $=$ 15 ms and a flip angle of 10° that had previously delivered high contrast from similar specimens. Axial images were obtained along the duodenum in a block of 32 slices of 1.2 mm thickness and separation, using a single excitation. The

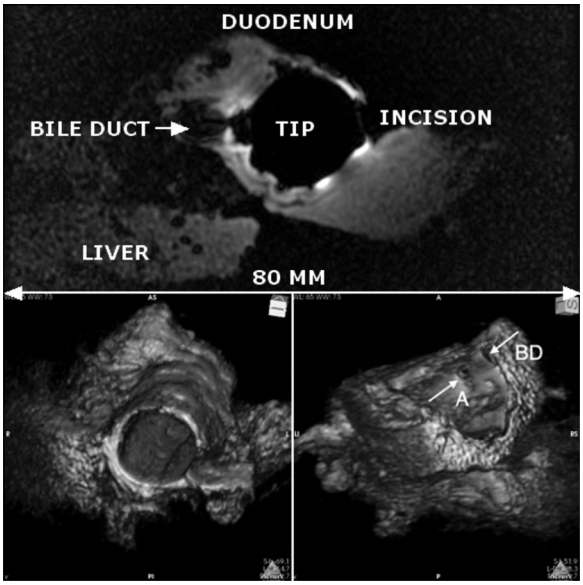

Fig. 11. Axial slice image of porcine liver specimen obtained using the duodenoscope receiver (upper), and 3-D reconstructions (lower). $1/R$ scaling has been applied to the duodenoscope axial image.

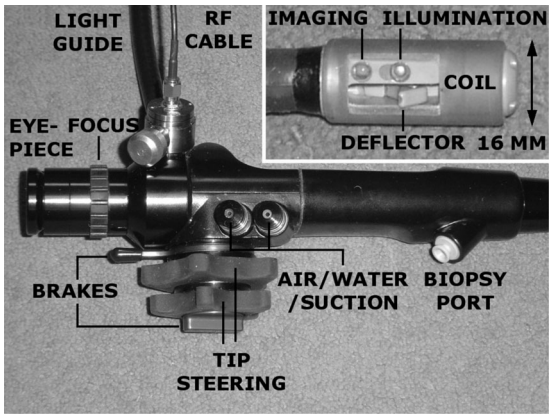

Fig. 12. Operating handle and tip of completed instrument.

upper part of Fig. 11 shows a typical slice. Here the image resolution is 0.78125 mm/pixel, and the image bandwidth is 92.968 Hz/pixel. The duodenoscope tip is located in the central dark region and is surrounded by duodenum with the bile duct on the left, the surgical incision on the right, and the underlying liver tissue below. Bright spots indicate modest overexcitation in the immediate vicinity of the coil conductors. Despite this, the image quality is generally good, and high-contrast imaging is achieved out to a useful distance. The lower image shows 3-D reconstructions obtained from such images, which allow the ampulla (A) and bile duct (BD) to be identified unambiguously.

F. Completed Instrument

A side-viewing duodenoscope incorporating the receiver design mentioned earlier was then constructed as shown in Fig. 12. To ensure MR compatibility, nonferrous materials such as polymers, titanium metal, and glass were used for the flexible elements, the actuation wires, pivots and fixtures, and the imaging components, respectively. The tip itself was fabricated in PEEK; construction was largely as previously described but with the addition of optical systems and an irrigation channel. RF signals were transmitted using the subminiature cable previously described, and an SubMiniature Version A-type connector was provided on the instrument handle. The electrical performance of the instrument was evaluated using a network analyzer and found to be substantially the same as that of the dummy used for development (with a loaded Q-factor of 28 and a signal rejection ratio of 36 dB in air).

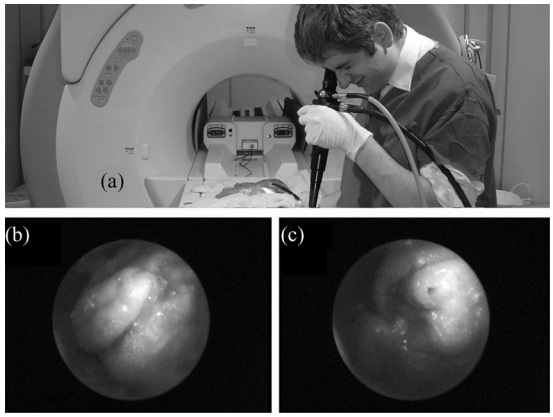

Fig. 13. (a) Optical imaging in the magnet room; images of (b) torus pyloricus and (c) ampulla of *ex-vivo* porcine liver specimen.

The flexible light guide was made over-length, to allow the placement of a SN LB-24 tungsten filament light source (Welch Allyn, Skaneateles Falls, NY, USA) in the scanner control room. An eyepiece and a WAT-231 S MR-compatible video camera (Watec, Orangeburg, NY, USA) were provided for viewing. The umbilical was also made over-length, to allow connection to air and suction services at the wall of the magnet room rather than a standard service cart. Water was delivered from a MD-431 bottle (Olympus).

The duodenoscope was evaluated in the magnet room, and no magnetic forces were observed. Optical images of *ex vivo* porcine liver specimens were obtained by a clinician using the eyepiece and also using the video camera as shown in Fig. 13(a); examples of image quality are shown in Fig. 13(b) and (c). The latter were transmitted to a PC in the scanner control room and then projected on a screen in the magnet room.

Susceptibility effects and decoupling were observed by placing the instrument on a cuboid phantom, with the shaft parallel to the magnet axis, and obtaining MR images using the system body coil. Little image disturbance was observed, suggesting that unwanted perturbations to the magnetization are small. Preliminary MR images were obtained using phantoms, in the arrangement described in Section III-D. Fig. 14(a) shows the experiment, and Fig. 14(b)–(d) show three consecutive axial slices from a block of 16 acquired in 1 min 9 s using a spin-echo sequence with TE = 10.488 ms and TR = 520 ms, 1 NEX, 5 mm slice thickness, 5.5 mm slice separation, and 160 mm FOV. The slice position ranges from the important deflector region [see Fig. 14(b)] to the distal tip [see Fig. 14(c)]. Image quality is excellent in the former case, with a peak SNR of 250,

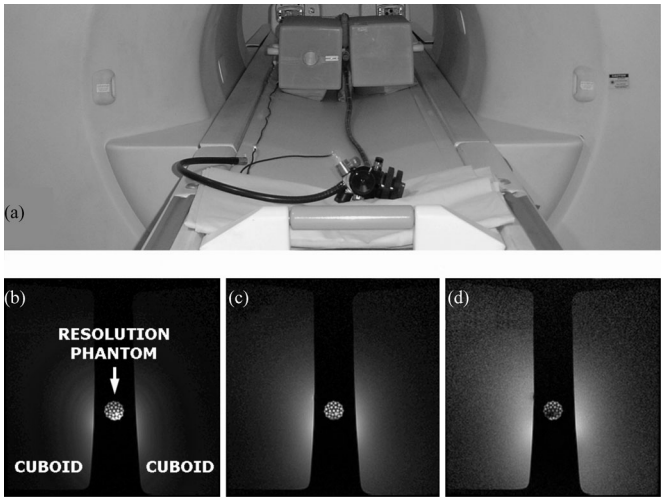

Fig. 14. (a) MR imaging trial of completed instrument; (b)–(d) consecutive axial slice images of phantoms, with $1/R$ scaling applied.

but degrades slightly in the latter case due to the short-range artifacts associated with the internal coil. These preliminary experiments demonstrate useful performance from the completed instrument, and *in vivo* human imaging trials are planned as soon as ethics approval has been obtained.

IV. Conclusion

An MR-imaging, side-viewing duodenoscope with full optical and mechanical functionality has been demonstrated. The instrument is intended for MR guidance of ERCP and high-resolution imaging of the biliary ductal system. The instrument is constructed from MR-compatible materials and combines a coherent fiber bundle for optical imaging, an irrigation channel, and a side-opening biopsy channel for the passage of catheter tools with a saddle coil for MR signal reception. The receiver coil is magnetically coupled to an internal pickup coil for intrinsic safety, and the system is tuned, matched, and decoupled using the minimum of internal components. The instrument is designed for ^{1}H imaging in 1.5 T fields, and allows high-quality images to be obtained over a wide field of view. The instrument has been evaluated in a conventional MR imaging suite using phantoms and *ex vivo* animal tissue and allows optical and MR images to be combined without loss of clinical functionality.

Further study is required to demonstrate safety and clinical utility before an application is made for ethics approval for human trials. For example, evaluation of the effects of motion artefacts during *in vivo* imaging is required. A significant difference between the artefacts obtained using external coils and the MR-imaging duodenoscope are to be expected, since the target tissue is likely to be comoving with the receiver in the latter case. In addition, it will be important to demonstrate that improvements in cannulation success rates can be achieved using MR rather than optical imaging and that high-resolution MR images of greater diagnostic value than fluoroscopic images can be obtained.

Acknowledgment

The authors would like to thank Prof. C. Besant and Dr. M. Ristic for many valuable discussions, Endoscan for the construction of the duodenoscope, P. Jones and Dr. M. Ahmad for workshop support, and Prof. W. Gedroyc for access to MRI facilities.

References

[1] J. A. Rider, E. J. Puletti, and H. C. Moeller, "The fiber duodenoscope: A preliminary report," *Amer. J. Gastroenterol*., vol. 47, pp. 21–27, Jan. 1967.
[2] I. Oi, "Fiberduodenoscopy and endoscopic pancreatocholangiography," *Gastrointest. Endosc*., vol. 17, pp. 59–62, Nov. 1970.
[3] K. Takagi, S. Ikeda, Y. Nakagawa, N. Sakaguchi, and T. Takahashi, "Retrograde pancreatography and cholangiography by fiber duodenoscope," *Gastroenterology*, vol. 59, pp. 445–452, Sep. 1970.
[4] J. A. Vennes and S. E. Silvis, "Endoscopic visualization of bile and pancreatic ducts," *Gastrointest. Endosc*., vol. 18, pp. 149–152, May 1972.
[5] O. T. Nebel and M. F. Fornes, "Endoscopic pancreatocholangiography," *Amer. J. Dig. Dis*., vol. 18, pp. 1042–1050, Dec. 1973.
[6] W. R. Brugge and J. Van Dam, "Pancreatic and biliary endoscopy," *New Engl. J. Med*., vol. 341, pp. 1808–1816, Dec. 1999.
[7] R. Kozarek, "Biliary ERCP," *Endoscopy*, vol. 39, pp. 11–16, Jun. 2007.
[8] L. Safrany, "Duodenoscopic sphincterotomy and gallstone removal," *Gastroenterology*, vol. 72, pp. 338–343, Feb. 1977.
[9] P. B. Cotton, "Non-operative removal of bile duct stones by duodenoscopic sphincterotomy," *Brit. J. Surg*., vol. 67, pp. 1–5, Jan. 1980.
[10] P. B. Cotton, "Duodenoscopic placement of biliary prostheses to relieve malignant obstructive jaundice," *Brit. J. Surg*., vol. 69, pp. 501–503, Sep. 1982.
[11] K. Huibregtse and G. N. Tygat, "Palliative treatment of obstructive jaundice by transpapilliary introduction of large bore bile duct endoprosthesis," *Gut*, vol. 23, pp. 371–375, May 1982.
[12] C. D. Anderson, C. W. Wright Pinson, J. Berlin, and R. S. Chari, "Diagnosis and treatment of cholangiocarcinoma," *Oncologist*, vol. 9, pp. 43–57, Feb. 2004.
[13] A. Parodi, D. Fisher, M. Giovannini, T. Baron, and M. Conio, "Endoscopic management of hilar cholangiocarcinoma," *Nature Rev. Gastroenterol. Hepatol*., vol. 9, pp. 105–112, Feb. 2012.
[14] R. P. Venu, J. E. Geenen, M. Kini, W. J. Hogan, M. Payne, G. K. Johnson, and M. J. Schmalz, "Endoscopic retrograde brush cytology: A new technique," *Gastroenterology*, vol. 99, pp. 1475–1479, Nov. 1990.
[15] I. C. Roberts-Thomson and J. B. Hobbs, "Cytodiagnosis of pancreatic and biliary cancer by endoscopic duct aspiration," *Med. J. Aust*., vol. 1, pp. 370–372, May 1979.
[16] N. Fujita, Y. Noda, G. Kobayashi, K. Kimura, and K. Ito, "Endoscopic approach to early diagnosis of pancreatic cancer," *Pancreas*, vol. 28, pp. 279–281, Apr. 2004.
[17] K. Huibregtse, R. M. Katon, P. P. Coene, and G. N. J. Tytgat, "Endoscopic palliative treatment in pancreatic cancer," *Gastrointest. Endosc*., vol. 32, pp. 334–338, Oct. 1986.
[18] W. S. McCune, P. E. Shorb, and H. Moscovitz, "Endoscopic cannulation of the ampulla of Vater: A preliminary report," *Ann. Surg*., vol. 167, pp. 752–756, May 1968.
[19] P. B. Cotton, L. H. Blumgart, G. T. Davies, J. W. Pierce, P. R. Salmon, R. J. Burwood, B. W. Lawrie, and A. E. Read, "Cannulation of papilla of Vater via fiber-duodenoscope: Assessment of retrograde cholangiopancreatography in 60 patients," *Lancet*, vol. 299, pp. 53–58, Dec. 1972.
[20] M. L. Freeman, J. A DiSario, D. B. Nelson, M. B. Fennerty, J. G. Lee, D. J. Bjorkman, C. S. Overby, J. Aas, M. E. Ryan, G. S. Bochna, M. J. Shaw, H. W. Snady, R. V. Erickson, J. P. Moore, and J. P. Roel, "Risk factors for post-ERCP pancreatitis: A prospective, multicenter study," *Gastrointest. Endosc*., vol. 54, pp. 425–434, Oct. 2001.
[21] E. L. A. Artifon, P. Sakai, J. E. M. Cunha, B. Halwan, S. Ishioka, and A. Kumar, "Guidewire cannulation reduces risk of post-ERCP pancreatitis and facilitates bile duct cannulation," *Amer. J. Gastroenterol*., vol. 102, pp. 2147–2153, Oct. 2007.
[22] H. I. Goldberg, M. K. Bilbao, E. T. Stewart, C. A. Rohrmann, and A. A. Moss, "Endoscopic retrograde cholangiopancreatography: Radiographic technique," *Amer. J. Dig. Dis*., vol. 21, pp. 270–278, Mar. 1976.
[23] B. K. Wallner, K. A. Schumacher, W. Weidenmaier, and J. M. Friedrich, "Dilated biliary tract: Evaluation with MR cholangiography with a T2-

weighted contrast enhanced fast sequence," *Radiology*, vol. 181, pp. 805–808, Dec. 1991.
[24] J. Laubenberger, M. Büchert, B. Schneider, U. Blum, J. Hennig, and M. Langer, "Breath-hold projection magnetic resonance-cholangio pancreatography (MRCP): A new method for the examination of the bile and pancreatic ducts," *Magn. Reson. Med.*, vol. 33, pp. 18–23, Jan. 1995.
[25] P. A. Bottomley, E. Atalar, R. F. Lee, K. A. Shunk, and A. Lardo, "Cardiovascular MRI probes for the outside in and for the inside out," *Mag. Res. Mater. Phys., Biol. Med.*, vol. 11, pp. 49–51, Jan. 2000.
[26] C. R. Weiss, C. Georgiades, L. V. Hofmann, R. Schulick, M. Choti, P. Thuluvath, D. A. Bluemke, and A. Arepally, "Intrabiliary MR imaging: Assessment of biliary obstruction with the use of an intraluminal MR receiver coil," *J. Vasc. Interv. Radiol.*, vol. 17, pp. 845–853, May 2006.
[27] K. Inui, S. Nakazawa, J. Yoshino, K. Yamao, H. Yamachika, T. Wakabayashi, N. Kanemaki, and H. Hidano, "Endoscopic MRI: Preliminary results of a new technique for visualization and staging of gastrointestinal tumors," *Endoscopy*, vol. 27, pp. 480–485, Sep. 1995.
[28] K. Inui, S. Nakazawa, J. Yoshino, and H. Ukai, "Endoscopic MRI," *Pancreas*, vol. 16, pp. 413–417, Apr. 1998.
[29] D. R. Feldman, D. Kulling, R. H. Hawes, C. L. Kay, V. R. Muckenfuss, P. B. Cotton, D. E. Bohning, and J. W. Young, "MR endoscopy: Preliminary experience in human trials," *Radiology*, vol. 202, pp. 868–870, Mar. 1997.
[30] D. Kulling, D. R. Feldman, C. L. Kay, B. J. Hoffman, C. E. Reed, J. W. Young, and R. H. Hawes, "Local staging of esophageal cancer using endoscopic magnetic resonance imaging: Prospective comparison with endoscopic ultrasound," *Endoscopy*, vol. 30, pp. 745–749, Nov. 1998.
[31] T. Ichikawa, F. Kitahara, T. Araki, A. Nanbu, M. Hori, H. Kumagai, S. Aoki, and M. Fujino, "MR endoscopy: Results in applying to the upper gastrointestinal and pancreatobiliary tracts," in *Proc. 9th Ann. Conf. ISMRM*, Glasgow, U.K., Apr. 21–27, 2001, vol. 9, p. 2043.
[32] Y. Matsuoka, K. Kuroda, E. Kumamoto, A. Saito, T. Mine, T. Shibasaki, and B. Keserci, "An integrated MR-endoscope for diagnosis of luminal organ," in *Proc. 12th Ann. Conf. ISMRM*, Kyoto, Japan, May 15–21, 2004, vol. 12, p. 969.
[33] Y. Matsuoka, T. Ozaki, Y. Mori, K. Murakami, M. Matsumoto, E. Kumamoto, K. Imagawa, M. Gotanda, and K. Kuroda, "Development of RF coil for integration system of endoscope for esophageal examination," in *Proc. 14th Ann. Conf. ISMRM*, May 6–12, 2006, vol. 14, p. 1405.
[34] N. M. DeSouza, A. H. Gibbons, A. S. Hall, R. Puni, J. Calam, and I. R. Young, "Magnetic resonance imaging during upper GI endoscopy: Technical considerations and clinical feasibility," *Min. Invas. Ther. All. Tech.*, vol. 4, pp. 277–281, Jan. 1995.
[35] N. M. DeSouza, G. A. Coutts, D. J. Larkman, D. J. Gilderdale, A. D. Williams, A. Thillainagayam, and I. R. Young, "Combined MRI and fibreoptic colonoscopy: Technical considerations and clinical feasibility," *Min. Invas. Ther. All. Tech.*, vol. 9, pp. 25–30, Jan. 2000.
[36] D. J. Gilderdale, A. D. Williams, U. Dave, and N. M. DeSouza, "An inductively-coupled, detachable receiver coil system for use with magnetic resonance compatible endoscopes," *JMRI*, vol. 18, pp. 131–135, Jul. 2003.
[37] J. L. Ackerman, E. Nevo, E. J. Zucker, A. J. Poitzsch, K. Vandenberg, A. Zhigalin, and B. Fetics, "MR endoscope with software-controlled tuning, device tracking and video," in *Proc. 19th Ann. Conf. ISMRM*, Montréal, QC, Canada, May 7–13, 2011, vol. 19, p. 4544.
[38] D. M. Ginsberg and M. J. Melchner, "Optimum geometry of saddle shaped coils for generating a uniform magnetic field," *Rev. Sci. Inst.*, vol. 41, pp. 122–123, Jan. 1970.
[39] A. J. Martin, D. B. Plewes, and R. M. Henkelman, "MR imaging of blood vessels with an intravascular coil," *JMRI*, vol. 2, pp. 421–229, Jul./Aug. 1992.
[40] B. C. Johnson, "Electrical resistance of copper and nickel thin film connections," *J. Appl. Phys.*, vol. 67, pp. 3018–3024, Mar. 1990.
[41] M. K. Konings, L.W. Bartels, H. F. M. Smits, and C. J. G. Bakker, "Heating around intravascular guidewires by resonating RF waves," *JMRI*, vol. 12, pp. 79–95, Jul. 2000.
[42] D. I. Hoult and R. E. Richards, "The signal-to-noise ratio of the magnetic resonance experiment," *J. Magn. Reson.*, vol. 24, pp. 71–85, Oct. 1976.
[43] C. E. Hayes, W. A. Edelestein, J. F. Schenck, O. Mueller, and M. Eash, "An efficient, highly homogeneous radiofrequency coil for whole-body NMR imaging at 1.5 T," *J. Magn. Reson.*, vol. 63, pp. 622–628, Jul. 1985.
[44] M. M. Swindle, *Swine in the Laboratory: Surgery, Anesthesia, Imaging and Experimental Techniques*, 2nd ed. Boca Raton, FL, USA: CRC Press, 2007.

Richard R. A. Syms (SM'02) received the B.A. degree in 1979 and the D.Phil. degree in 1982 from Oxford University, Oxford, U.K., both in engineering science. He is currently a Professor of Microsystems Technology in the EEE Department, Imperial College London, London, U.K., where he leads the Optical and Semiconductor Devices Group. He has authored or coauthored more than 200 journal and conference papers on optics, electromagnetic theory, microelectromechanical systems, metamaterials, and medical imaging.

Prof. Syms is a Fellow of the Royal Academy of Engineering, the Institute of Electrical Engineers, and the Institute of Physics.

Ian R. Young received the B.Sc. degree in 1954 and the Ph.D. degree in 1958 from Aberdeen University, Aberdeen, U.K., both in physics. He is currently a Senior Research Fellow in the EEE Department, Imperial College London, London, U.K. He has authored or coauthored more than 300 papers on MRI. His current research interests include *in vivo* magnetic resonance imaging (MRI) and MR-guided surgical robots.

Prof. Young is a Fellow of the Royal Society and a Fellow of the Royal Academy of Engineering and a winner of the Gold Medal of SMRM and the Sir Frank Whittle Prize.

Christopher A. Wadsworth received the Graduate degree in medicine from St. George's University London, London, U.K., and the Ph.D. degree from Imperial College London, London, in 2012, for his work into the investigation of bile duct cancer.

He completed his medical training in North West London. He is a currently a Gastroenterologist and is the Advanced HPB Endoscopy Fellow at Aintree University Hospitals NHS Trust.

Simon D. Taylor-Robinson received the M.B.B.S. degree in 1984 from London University, London, U.K. He is currently the Dean of the Faculty of Medicine of Imperial College and the Director of the Hepatology Clinical Research Facility, St Mary's Hospital, London. He has built up the largest dedicated viral hepatitis treatment centre in Europe. He also has research programs looking into progression of liver fibrosis and has collaborated with the Engineering Faculty at Imperial on EPSRC, Wellcome, and National Institute for Health Research grants to produce new medical imaging devices.

Marc Rea received the Ph.D. degree from the Imperial College, London, U.K., in 2010, on MR-compatible systems for prostate biopsy.

He is currently a Clinical Scientist at St. Mary's Hospital, London. His current research interests include medical robotics, magnetic resonance imaging (MRI)-compatible device tracking, and high-intensity focused ultrasound.